Untangling the Annual Cycle of the Tropical Tropopause Layer with an Idealized Moist Model

M. JUCKER[a] AND E. P. GERBER

Courant Institute of Mathematical Sciences, New York University, New York, New York

(Manuscript received 26 February 2017, in final form 1 June 2017)

ABSTRACT

The processes regulating the climatology and annual cycle of the tropical tropopause layer (TTL) and cold point are not fully understood. Three main drivers have been identified: planetary-scale equatorial waves excited by tropical convection, planetary-scale extratropical waves associated with the deep Brewer–Dobson circulation, and synoptic-scale waves associated with the midlatitude storm tracks. In both observations and comprehensive atmospheric models, all three coexist, making it difficult to separate their contributions. Here, a new intermediate-complexity atmospheric model is developed. Simple modification of the model's lower boundary allows detailed study of the three processes key to the TTL, both in isolation and together.

The model shows that tropical planetary waves are most critical for regulating the mean TTL, setting the depth and temperature of the cold point. The annual cycle of the TTL, which is coldest (warmest) in boreal winter (summer), however, depends critically on the strong annual variation in baroclinicity of the Northern Hemisphere relative to that of the Southern Hemisphere. Planetary-scale waves excited from either the tropics or extratropics then double the impact of baroclinicity on the TTL annual cycle. The remarkably generic response of TTL temperatures over a range of configurations suggests that the details of the wave forcing are unimportant, provided there is sufficient variation in the upward extent of westerly winds over the annual cycle. Westerly winds enable the propagation of stationary Rossby waves, and weakening of the subtropical jet in boreal summer inhibits their propagation into the lower stratosphere, warming the TTL.

1. Introduction

The tropopause, the separation between the troposphere and stratosphere, is markedly less distinct in the tropics than the extratropics (e.g., Highwood and Hoskins 1998). The atmosphere gradually transitions from a clearly tropospheric regime at 12 km, where convective towers tightly couple air masses to the surface, to a stratospheric regime above the tropical cold point near 17 km, where air parcels are months removed from the surface, extremely dry, but now richer in ozone. The notion of a tropical tropopause as a transition zone, as opposed to a distinct surface, appears in temperature and water vapor observations by Atticks and Robinson (1983), and the region has become known as the tropical

tropopause layer (TTL) [see Fueglistaler et al. (2009) for a comprehensive review].

The TTL also marks a transition between dynamical regimes. Below, the Hadley cell homogenizes angular momentum, allowing for a thermally driven overturning circulation. Above, the atmosphere lies in a downward control regime, where a mechanical torque (wave breaking) is necessary to drive a circulation across angular momentum surfaces. Following Fueglistaler et al. (2009), we define the TTL top around 18.5 km (70 hPa), where the observed lapse rate reaches its minimum. The bottom of the TTL might best be located around 14 km (150 hPa), the level of zero net radiative heating. Above this point, radiative warming balances the mechanically driven uplift of parcels into the stratosphere, while below it, convective heating plays a critical role.

The TTL is of crucial importance for the chemical composition of the stratosphere (e.g., Plumb 2007; Schofield et al. 2011; Randel and Jensen 2013). It is the entry point for most air that enters the stratosphere. Quasi-horizontal mixing of air and chemical tracers along isentropic surfaces transports air between the TTL and

[a] Current affiliation: School of Earth Sciences and Centre of Excellence for Climate System Science, The University of Melbourne, Australia

Corresponding author: Martin Jucker, publications@martinjucker.com

the "middle world," the lower stratosphere of the extratropics that laterally borders the TTL (Konopka et al. 2010; Ploeger et al. 2012; Abalos et al. 2013). In addition, the diabatic circulation brings air up through the top of the TTL into the "overworld," the isentropic layers of the middle atmosphere that never intersect the tropopause (Holton et al. 1995). Freeze-drying of air by the cold point strongly constrains water vapor throughout the stratosphere, especially for the overworld (Brewer 1949).

Solomon et al. (2010) highlight the role of the TTL on surface climate: modulations of stratospheric water vapor impact surface temperatures on decadal time scales. Dessler et al. (2013) suggest that processes in the TTL increase the climate sensitivity of the planet, with greenhouse gas forcing leading to an overall increase in water vapor throughout the stratosphere, which in turn enhances surface warming.

In this study, we develop a model of an idealized moist atmosphere to understand the processes regulating the climatology of the TTL, and in particular its striking *annual* cycle. Despite the semiannual variation of insolation across the tropics, the TTL exhibits a strong annual variation of up to 8 K (Chae and Sherwood 2007; Fueglistaler et al. 2009), in phase with the annual cycle of the boreal hemisphere. While the maximum annual cycle in temperature is located above the cold point, there is sufficient variation at this level to modulate stratospheric water vapor on an annual basis, the signal carried up by the diabatic circulation in what is known as the "stratospheric tape recorder" (Mote et al. 1996).

Comprehensive models are broadly (but not universally) able to capture this annual cycle in temperature (e.g., Gettelman et al. 2010), but the exact mechanisms are still the subject of active research. The bulk of the annual cycle in the TTL is directly forced by a seasonal variation in upwelling: stronger ascent in boreal winter cools the TTL through an increased rate of adiabatic expansion. The seasonal variation in upwelling also indirectly regulates temperature by driving variation of ozone and water vapor. Stronger upwelling in boreal winter reduces the concentration of ozone, leading to radiative impact of 1 to 2 K (Fueglistaler et al. 2011). A more recent study by Ming et al. (2017) takes into account annual variations in water vapor concentration as well, suggesting that total changes in ozone and water vapor could explain up to about 30% of temperature variations.

The open question is then this: What drives increased upwelling in boreal winter? Yulaeva et al. (1994) observed nearly complete compensation between MSU-4 lower stratosphere temperature anomalies in the tropics versus the extratropics, and related them to changes in the stratospheric meridional overturning circulation. As the meridional overturning is dominated by the winter

hemisphere, they suggested that the stronger orographic and thermal forcing of planetary waves in the Northern Hemisphere relative to the Southern Hemisphere would drive stronger upwelling in boreal winter compared to austral winter. Although Fueglistaler et al. (2011) note that the compensation in MSU-4 data was somewhat fortuitous, Ueyama and Wallace (2010) found that tropical upwelling in the Brewer–Dobson circulation (BDC) is correlated to eddy heat fluxes at high latitudes, more so than with equatorial tropospheric planetary waves. Chen and Sun (2011) and Gerber (2012) also showed evidence for a link between extratropical planetary waves and TTL upwelling at the cold point in idealized atmospheric models.

Other studies, however, have found that extratropical planetary waves, while important for upwelling above 70 hPa, matter much less in the TTL (Chae and Sherwood 2007; Ueyama et al. 2013). This suggests the need for a more local, tropical mechanism. Kerr-Munslow and Norton (2006) and Norton (2006) explore the influence of the Indian monsoon on the TTL temperature and upwelling annual cycle. Their wave analysis and numerical experiments suggest that the annual cycle is forced by the breaking of equatorial Rossby waves due to tropical convection close to the tropopause.

Along the same lines, Boehm and Lee (2003) report that the order of magnitude of tropical upwelling can be explained with tropical convection–induced Rossby waves. However, they also find that those waves result in stronger upwelling in July rather than January, contrary to observed upwelling. Randel et al. (2008) show that different wave sources contribute in different ways to the tropical upwelling. Whereas extratropical waves are important in the mean upwelling at 100 hPa, the seasonal cycle seems to be largely linked to shifting convection. These authors also attribute the annual cycle to horizontal eddy momentum flux convergence coming from both extratropical and tropical waves. The findings of Grise and Thompson (2013) point into the same direction: high-vertical-resolution GPS radio occultation data show that equatorial planetary waves dominate the zonally asymmetric TTL temperature components, but that TTL variability is determined by both equatorial and extratropical tropospheric waves.

Ortland and Alexander (2014) confirm that equatorial Rossby waves driven by convection drive most of the tropical upwelling in the mean, but propose another mechanism for the annual variation. Rather than changes in the location or intensity of convection, they suggest that changes in the refractive index due to mean wind variations can filter and reorient different waves at different times of the year. Hence there can be an annual cycle in upwelling driven by convectively generated waves even if the convection itself is constant.

Finally, Jucker et al. (2013), propose a third mechanism for the TTL annual cycle, focused on asymmetry in synoptic variability. They found that both the structure and magnitude of the difference between January and July TTL could be obtained in a dry model without convection. The only requirement in such a model is that extratropical meridional temperature gradients have a larger annual cycle in the Northern than in the Southern Hemisphere troposphere, suggesting a large impact of extratropical baroclinicity in setting up the TTL structure.

This work tests the three key elements of these theories in the simplified framework of a new idealized model, detailed in section 2. The representation of the key forcings—tropical planetary waves, extratropical planetary waves, and variations in baroclinicity and synoptic waves—and their impact on mean TTL structure are discussed in section 3. Section 4 explores their impacts on the annual cycle in the TTL, highlighting the importance of nonlinear interaction between the different forcings. We then explore the mechanism(s) in detail in section 5, and finally summarize and conclude the manuscript in section 6. In support of the results of Randel et al. (2008) and Grise and Thompson (2013), we find an important role for all waves in the TTL, but show that variations in the tropical winds—as identified by Ortland and Alexander (2014)—are critical for regulating their annual variations.

2. A model of an idealized moist atmosphere: MiMA

Idealized models of the atmosphere serve as intermediaries between the real atmosphere and our conceptual understanding (Held 2005). While idealization comes at the expense of a more realistic representation of the atmosphere, simplicity permits greater transparency and control of the key processes driving the circulation. In this study, the chief idealization will be to neglect the role of cloud and aerosol processes. Building on Merlis et al. (2013a), we explore an idealized atmosphere where moisture interacts with the circulation through the transport of latent heat (both through parameterized convection and resolved transport) and interacts with radiative transfer, but only in vapor form. The model provides a new step in a hierarchy of models, linking more idealized general circulation models (GCMs) with comprehensive atmospheric models.

Among the simplest GCMs in this hierarchy are the so-called dry dynamical cores, which are primitive equation solvers on the sphere driven by a highly simplified representation of atmospheric physics (e.g., Held

and Suarez 1994; Polvani and Kushner 2002; Schneider and Walker 2006; Jucker et al. 2013). They have proven a useful tool for understanding the natural variability of the atmosphere (e.g., Gerber and Vallis 2007; Chen and Plumb 2009; Jucker 2016) and its response to external forcing (e.g., Simpson et al. 2009; Butler et al. 2010; Kidston et al. 2011). Even with highly simplified climate physics—all processes associated with radiation and moisture are parameterized by a simple Newtonian relaxation to a given "equilibrium" temperature profile—such models are capable of capturing, at least qualitatively, the formation and response of the tropical cold point to large-scale perturbations in the climatological forcing (Gerber 2012; Kim and Son 2015). In particular, Ryu et al. (2008) and Ryu and Lee (2010) explore the impact of planetary-scale tropical waves on the cold point in a dry dynamical core by approximating convection through localized heating anomalies in the tropics. They show how Kelvin waves influence the variability and intensity of the "cold trap," the coldest region of the TTL over the western Pacific.

In this work, we are keenly interested in the role of tropical convection and the annual cycle of solar insolation on the TTL, necessitating additional physics in the model. Frierson et al. (2006, 2007; note that "FHZ" is used herein to refer to the ideas presented in both papers, which are parts 1 and 2 of a single work) provide a step in this direction, adding prognostic moisture to the large-scale circulation, and developing the necessary changes to the boundary layer and surface for energetic consistency. To explicitly remove the radiative impacts of water vapor (and thus allow greater changes in the role of latent heat transport without radiative feedbacks), they introduced a "gray radiation" scheme where a single spectral band of longwave radiation interacts with specified optical thickness, independent of the time-varying water vapor in the atmosphere. While the model captures the key influence of synoptic variability on the tropopause structure (Haqq-Misra et al. 2011), the gray radiation approximation leads to significant problems in the stratosphere, where the radiative damping time scales become unrealistically long and shortwave heating associated with ozone plays a critical role in the circulation.

Merlis et al. (2013a,b) build on FHZ by replacing the gray radiation scheme with a full radiative transfer, using the scheme employed by GFDL's Atmospheric Model 2 (AM2; Delworth et al. 2006). We follow in their direction, developing the Model for an Idealized Moist Atmosphere (MiMA). MiMA essentially uses the physics of FHZ, but replaces the gray radiation with a full radiation scheme, namely the GCM version of the Rapid Radiative Transfer Model (RRTM) (Mlawer
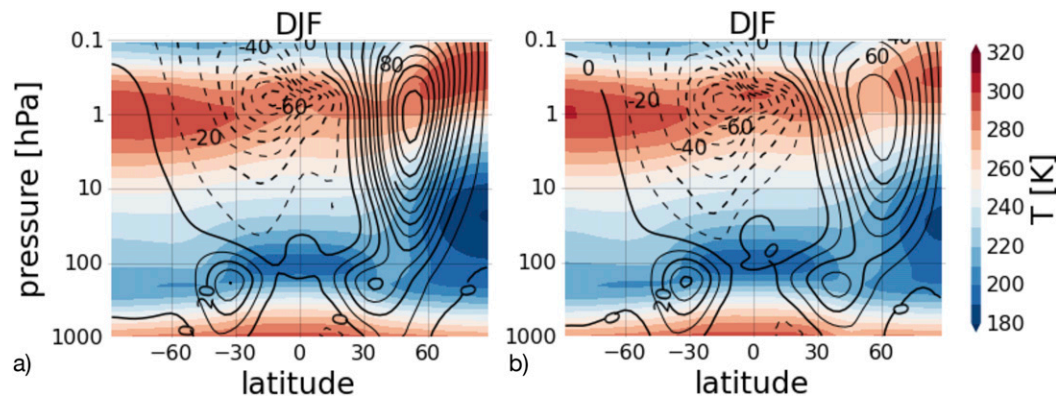
FIG. 1. Control climatological DJF zonal mean zonal wind (contours, interval $10\,\mathrm{m\,s^{-1}}$) and temperature (shading). (a) The control run is north–south symmetric, with a uniform slab ocean with mixed layer depth 100 m (CTRL in Table 1). (b) For comparison, the DJF climatology of a simulation with wave-1 4-km topography and 1-m midlatitude "land" is shown (L01.O4M1 in Table 1). The polar vortex weakens by about 40% when adding this additional forcing in the NH midlatitudes.

et al. 1997; Iacono et al. 2000). Because of the full treatment of radiation, some adjustments had to be made to the surface mixed layer ocean and stratosphere, as detailed below.

In particular, clouds have a net cooling impact on the atmosphere, such that a cloud-free atmosphere with equivalent greenhouse gas concentrations (here just carbon dioxide and water vapor) will be notably warmer than an atmosphere with realistic cloud coverage. Merlis et al. (2013a) address this problem by specifying a time-invariant cloud distribution. As the net cooling effect of clouds is predominantly in the extratropics (where clouds are lower, such that the shortwave cooling influence outweighs their longwave warming influence), their cloud distribution helps maintain temperature contrast between the tropics and high latitudes. Cloud forcings, however, strongly influence the circulation (e.g., Voigt and Shaw 2015).

To avoid constraining the position of the extratropical jets, we explicitly leave clouds entirely out of the model. To compensate for cloud's net cooling effect, we increase the surface albedo to maintain a reasonable climatology. The surface albedo does allow for considerable freedom in regulating the model's climate; for instance, a latitude-dependent albedo can be used to modify the temperature contrast between tropics and extratropics, similar to the fixed cloud approach taken by Merlis et al. (2013a). In all simulations discussed here, however, we have opted for the simplest configuration: a globally uniform albedo without any spatial structure.

A fairly limited set of parameters (detailed in the remainder of this section and the next) allows one to explore a wide range of atmospheric circulation

regimes with MiMA, as shown in Fig. 1. The first panel illustrates a hemispherically symmetric aquaplanet simulation, our "control" climate, and the second, a more Earth-like configuration in which the north–south symmetry has been broken with the addition of zonal asymmetries and a crude approximation of land–sea contrast in the Northern Hemisphere. As shown in section 4, the simulation pictured on the left has no annual cycle in the TTL, while that on the right has an annual cycle comparable to the observed atmosphere.

The code is publicly available, and all results shown in this paper are based on MiMA release v1.0 (Jucker 2017). The exact technical details and extensive parameter descriptions can be found in the online documentation at https://mjucker.github.io/MiMA, and the key changes in MiMA relative to the FHZ and Merlis et al. (2013a) models are documented below. The default values to all parameters are given in the documentation folder inside the code repository at the URL given above. We list the most relevant parameter settings used in this work in Table 1 and the appendix (Table A1).

All simulations discussed in this work have been run with 80 hybrid vertical pressure levels. They are spaced in such a way to have 17 levels between 200 and 70 hPa for good resolution of the TTL. The horizontal resolution is T42. We have tested higher horizontal resolutions and found no significant differences in the region we are analyzing here. The spinup time is typically 20 years, followed by 10-yr simulations for analysis. Note that the spinup has been chosen rather long, as the stratospheric water vapor takes a long time to equilibrate, given that it is mainly governed by the slow transport of the Brewer–Dobson circulation.

TABLE 1. Overview of the model setups. "Albedo" corresponds to MiMA parameter const_albedo. "Topo" (km) corresponds to height and $m = 1(2)$ indicates the number of Gaussian mountains (1 or 2) in the NH midlatitudes. "Land" corresponds to land_capacity with $1\,\mathrm{m} = 4 \times 10^6\,\mathrm{J\,K^{-1}\,m^{-2}}$. "Warm pool" denotes the amplitude of zonal heat flux in $\mathrm{W\,m^{-2}}$, and T_{700} is the global mean temperature at 700 hPa in °C.

Name	Albedo (%)	Topo (km), m	Land (m)	Warm pool ($\mathrm{W\,m^{-2}}$)	T_{700} (°C)
CTRL	20.5	–	–	–	8.7
O2M1	20.5	2, 1	–	–	8.6
O4M1	20.5	4, 1	–	–	8.8
O2M2	20.5	2, 2	–	–	8.6
O4M2	20.5	4, 2	–	–	8.6
L50	20.7	–	50	–	8.7
L10	20.8	–	10	–	8.5
L01	21.0	–	1	–	8.8
W15	20.5	–	–	15	8.5
W30	19.7	–	–	30	8.7
W45	19.2	–	–	45	8.6
L01.O4M1	21.0	4, 1	1	–	8.8
L01.O4M2	21.0	4, 2	1	–	8.5
W30.O4M1	20.0	4, 1	–	30	8.5
W30.O4M2	19.8	4, 2	–	30	8.5
W30.L01	20.0	–	1	30	8.9
W30.L01.O4M1	20.5	4, 1	1	30	8.3
W30.L01.O4M2	20.3	4, 2	1	30	8.5

a. Radiative transfer

MiMA uses the GCM version of the RRTM code (RRTMG) for both shortwave and longwave radiative transfer calculations (Mlawer et al. 1997; Iacono et al. 2000). All parameters relating to clouds and aerosols are set to zero. RRTM can include water vapor, ozone, carbon dioxide, methane, nitrous oxide, oxygen (shortwave and longwave), and the halocarbons chlorofluorocarbon (CFC)-11, CFC-12, CFC-22, and CCl_4 (longwave only). In this work, however, we limit the radiative transfer calculations to three absorbers in the atmosphere: carbon dioxide, ozone, and water vapor. CO_2 is a simple scalar constant, set to 300 ppm throughout the atmosphere to roughly approximate its preindustrial concentration.

Ozone plays a fundamental role in the circulation of the stratosphere. In particular, the polar vortex in the winter hemisphere owes its existence largely to the meridional temperature gradient induced by shortwave absorption. In the simulations presented here, O_3 is specified by a time-invariant distribution which is zonally symmetric, but varies in latitude and pressure as illustrated in Fig. 2. This profile is based on the ozone climatology of Fortuin and Langematz (1994) but made north–south symmetric such that there is no ozone hole in the Southern Hemisphere, and the ozone concentrations in the Northern Hemisphere are somewhat too low compared to the real world. This allows us to focus
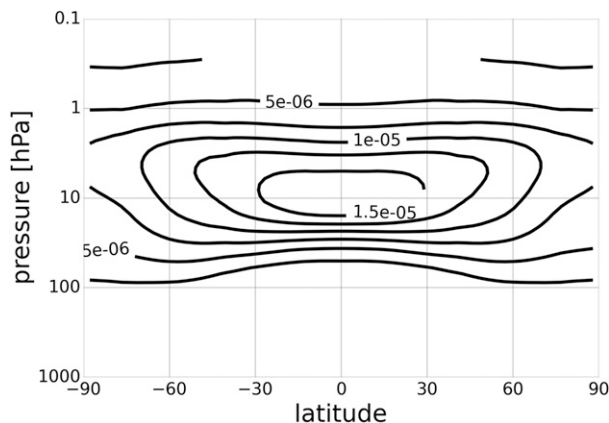

FIG. 2. Ozone distribution used in all simulations. MiMA reads ozone from an input file, which in our case contains a static and both zonally and north–south symmetric distribution based on the work of Fortuin and Langematz (1994). Contour interval is 2.5 ppm.

exclusively on the impact of hemispheric asymmetries in surface conditions on the TTL annual cycle. The north–south asymmetry of the stratosphere, however, could be improved with a more detailed treatment of ozone.

Figure 1a illustrates the winter and summer climatology of MiMA in its default configuration. Absent any zonal asymmetry in the lower boundary, the stratospheric vortex becomes extremely strong and steady in the winter hemisphere. When the zonal symmetry is broken at the surface, as illustrated in Fig. 1b, the vortex becomes more realistic and variable, exhibiting aperiodic sudden stratospheric warming events. The vortex remains strong relative to observed Northern Hemisphere, however, in part due to the strong meridional gradient in ozone (a consequence of symmetrizing the ozone profile) and the crude treatment of gravity waves by a Rayleigh friction (detailed below).

Water vapor is the final radiatively active gas in the model, prognostically determined through the hydrological cycle as in FHZ. All other potential absorbers are neglected, but can be trivially included with a constant scalar concentration, similar to the implementation of CO_2, or given a specified distribution in space and time, as with ozone. For more idealized experiments, one can also overwrite radiative transfer calculations entirely, reading in the radiative heating, surface fluxes, and water vapor from input files.

All of our simulations are run with a seasonal cycle based on a 360-day year of twelve 30-day months, the equinoxes at days 90 and 270. Although RRTM includes the possibility to compute the Earth–sun distance as a function of the day of the year, this calculation is only valid for 365-day years. Here, we fix the Earth–sun distance to 1 astronomical unit (AU), meaning that the Earth orbit is an exact circle; this allows us to focus exclusively on the

impact of surface conditions on asymmetry in the TTL annual cycle. The obliquity is fixed to 23.439°, and the solar constant to 1360 W m^{-2}. The radiative time step is 2 h.

In this study, we also apply diurnal averaging to the radiation scheme: the atmosphere always sees the daily mean radiation at all times, which varies only with latitude and the annual cycle. It is trivial to restore the diurnal cycle within in the code, but note that our decision to use diurnal averaging does impact the climate. If the diurnal cycle is turned on, one may need to adjust the surface albedo to minimize any changes to the climatology. Note that if running without diurnal averaging of the incoming SW flux, it is advisable to use a radiative time step that is not a divisor of a full day (such as 50 min). This is to avoid potential unphysical resonances when the radiation is called every day at the same time. We have checked that all the results presented here are independent of the choice of diurnal averaging, provided the albedo is adjusted as needed to maintain the same global mean temperature.

b. Water vapor and the hydrological cycle

The only active trace gas in MiMA is water vapor, which interacts with both shortwave and longwave radiation in RRTM. The surface fluxes, boundary layer, and large-scale condensation are exactly as described in FHZ. In addition, we include an idealized version of the convection scheme developed by Betts (1986) and Betts and Miller (1986), as implemented by Frierson (2007). Briefly, the scheme seeks to model both deep and shallow convection, and parameters are as given in the control simulation of Frierson (2007). Evaporation is determined through a simplified bulk physics boundary layer scheme, and the surface is modeled as an infinite reservoir of water vapor, exactly as in FHZ. Latent heat is released through large-scale condensation (which occurs whenever a grid box exceeds 100% relative humidity) or through the convection scheme. There are explicitly no clouds, so that precipitation falls out immediately, but it is evaporated again if it passes through any layer below that is unsaturated.

GFDL's dynamical core includes the possibility to correct the total water mass in the atmosphere after each integration step to ensure conservation by the advection scheme. While this scheme improves the energy balance of the atmosphere, it can introduce a systematic water vapor sink in the stratosphere as numerical errors coming from the troposphere (which holds the vast majority of the atmosphere water) alias into the stratosphere. To conserve stratospheric water vapor, the water mass correction scheme is only applied below a given pressure level, set by default to 200 hPa. The mass of water vapor above that level is smaller than 1% of the total mass, and

our testing has shown that the water vapor in the stratosphere is conserved without the correction scheme.

To ensure numerical stability of the radiative scheme, RRTM never sees specific humidity values below 0.2 ppmv, and the initial condition is set to 2 ppmv throughout the atmosphere. Note that both values are below typical values found anywhere in the stratosphere (except perhaps the southern stratospheric polar vortex), and the initial value is not important for the specific humidities found in the converged state of the model. In practice, these considerations are only relevant in the model spinup.

c. Surface conditions: A mixed layer ocean

The surface is modeled as a simple mixed layer, or "slab ocean," governed by an effective ocean heat capacity C_0 that can be varied in latitude and longitude. The temperature evolves as given in Eq. (1) of FHZ, repeated here for completeness:

$$C_O \frac{\partial T_S}{\partial t} = R_S - R_{Lu} + R_{Ld} - L_v E - S, \qquad (1)$$

with R_S, R_{Lu}, and R_{Ld} being the net shortwave, upward, and downward longwave fluxes, L_v the latent heat of vaporization, E evaporative flux, and S sensible heat flux. The latent and sensible heat fluxes are determined by a simplified bulk physics boundary layer scheme exactly as in FHZ.

The heat capacity C_0 and surface albedo (which influences the net shortwave radiation S) are the two key parameters regulating the surface. The heat capacity plays an essential role in the annual cycle, as detailed in section 3. The surface albedo is important for regulating the global mean surface temperature; clouds have a net cooling impact on the Earth, and a reasonable climatology in MiMA depends on tuning the surface albedo to compensate. As explained in detail in section 3, we adjust it for every experiment independently, to ensure that global mean temperatures near the surface are very similar across all simulations (see last column of Table 1).

As the mixed layer ocean does not allow any oceanic heat transport, a large part of the global meridional heat flux is missing, particularly in the tropics, where the ocean dominates atmospheric heat transport. If not addressed, this leads to strong meridional temperature gradient, and consequently, an unnaturally strong subtropical jet. To remedy this, we include a static surface heat flux, a so-called Q flux, to remove heat in the tropics and redistribute it in the extratropics. The form follows exactly the symmetric version of Merlis et al. (2013b), which models the divergence of the poleward ocean energy flux as

$$\nabla \cdot \mathbf{F}_O(\phi) = Q_0 \frac{1}{\cos\phi} \left(1 - \frac{2\phi^2}{\phi_0^2}\right) \exp\left(-\frac{\phi^2}{\phi_0^2}\right), \qquad (2)$$
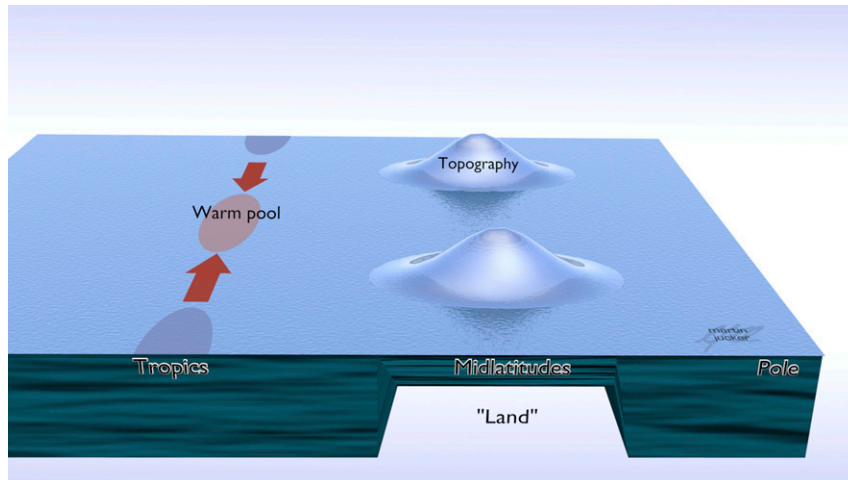
FIG. 3. The three key surface forcings used to modulate the TTL in MiMA. Extratropical planetary waves are excited by Gaussian-shaped mountains positioned in the midlatitudes. Tropical planetary waves are excited by a purely zonal heat flux within the tropics, which generates a "warm pool" (i.e., a localized region of maximum SSTs along the equator) that in turn drives zonal asymmetry in tropical convection. Last, synoptic variability is modulated by reducing the heat capacity of the mixed layer ocean in the midlatitudes of one hemisphere, a very crude approximation to "land," which in turn amplifies the annual cycle of midlatitude baroclinicity.

with $Q_0 = 30$ W/m^2 and $\phi_0 = 16°$ throughout this work. We found that a larger value produces a clear double-ITCZ structure in the tropics, whereas a lower value has a single intertropical convergence zone (ICTZ) but allows the subtropical jets to become too strong.

d. Upper boundary conditions

To approximate the effect of gravity wave drag on the upper stratosphere, and avoid wave reflection off the model top, we introduce a crude parameterization of gravity waves through a Rayleigh friction sponge layer above 0.5 hPa. This friction is exactly as described in Polvani and Kushner (2002) and has a time scale of 0.5 days at the top layer. This can be replaced with an interactive gravity wave scheme as detailed by Cohen et al. (2013), but the results of this study are largely insensitive to the gravity wave scheme, and the simple sponge layer was sufficient.

3. Capturing the key processes regulating the TTL in an idealized model

As detailed in the introduction, previous studies have identified three main players regulating upwelling in the TTL: extratropical planetary waves, tropical planetary waves, and midlatitude synoptic waves. The schematic in Fig. 3 provides an overview of how we introduce each into MiMA through modification of the surface conditions. This gives us three fairly

independent knobs to perturb the TTL and its annual cycle. Table 1 lists the 18 main simulations we will subsequently analyze with the naming conventions, and the values for each key forcings (albedo, topography, land–sea contrast, and warm pool). The last column shows the global mean temperature in the lower troposphere (700 hPa), which we used as a calibration point for all simulations.

Figure 4 shows the effects of each forcing on the tropical temperature profiles around the cold point, and presents the key results of this section: 1) MiMA can reasonably capture the structure of the TTL, as compared to ERA-I reanalyses and a comprehensive climate model with a well-represented stratosphere, and 2) tropical planetary waves excited by localized SST anomalies in the tropics are most effective of the three forcings in modifying the mean TTL. In fact, our tropical temperature only begins to reasonably match the observed profiles with inclusion of realistic asymmetry in tropical SSTs (Fig. 4a). Before discussing each of the forcings in detail, however, we explain the importance of using the planetary albedo of our model to steady the tropical SSTs across all integrations.

The annual cycle of the TTL is driven by variations in upwelling, but mean TTL temperatures are quite sensitive to surface temperatures. A perturbation to the tropical mean SSTs leads to a linear offset in TTL temperatures, which can be further amplified by moist lapse rate feedback: warmer SSTs increase the moisture
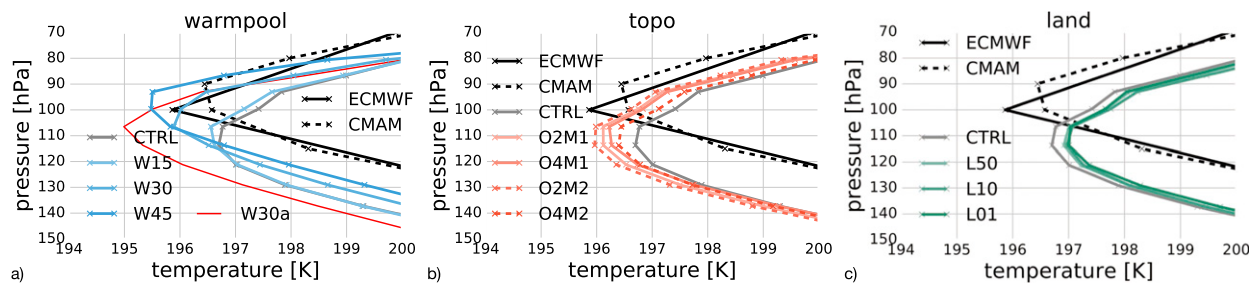
FIG. 4. Vertical temperature profiles of the tropical cold point region showing the effects of (a) the tropical warm pool, (b) midlatitude orographic forcing, and (c) extratropical land–sea contrast on the annual mean cold point structure. Temperatures were averaged from 30°S to 30°N to construct the profiles. The tropical warm pool has the largest effect on the annual mean, whereas extratropical land–sea contrast has the weakest effect. The fine red line in (a), labeled W30a, shows the temperature profile for a W30-like integration in which the surface albedo was left the same as in CTRL; see text for more discussion.

content of the atmosphere and thus a reduction of the lapse rate. For each perturbation experiment, we therefore retune the surface albedo to keep tropical SSTs exactly the same. This allows us to keep in an Earth-like regime in all experiments, and focus on the impact of the surface conditions on the upwelling in the TTL region, not on their influence on mean surface temperature.

For example, the impact of a zonal redistribution of heat within in the tropical mixed layer on the global mean temperature is illustrated in Fig. 4a. The ''W30a'' and ''W30'' integrations have identical setups, including a purely zonal $30 \, \mathrm{W \, m^{-2}}$ heat flux in the tropical mixed layer (as detailed in section 3a), except that integration W30a has default albedo of 0.205, whereas integration W30 has an adjusted albedo of 0.197. Even though the heat flux has no net zonal mean, just the introduction of zonal asymmetry to the tropical SSTs induces a 1.5-K *zonal mean* TTL cooling in integration W30a. This is associated with a cooling of the entire tropical troposphere that penetrates up into the upper troposphere and lower stratosphere (UTLS). In integration W30, however, the albedo was decreased from the control value of 0.205 to 0.197 to maintain the tropical mean surface temperature. The overall change in the TTL structure

induced by the heat flux is about the same in both integrations (e.g., the cold point rises relative to the control integration), but the W30 integration isolates the impact of the change in upwelling from that of the SST.

Table 1 lists the albedo correction that was applied to each perturbation experiment. We stress that the impact is strongest on the mean temperature of the TTL, but not so important for its structure or its annual cycle.

a. Planetary waves in the tropics: A simulated warm pool

The warm pool in the west Pacific and Maritime Continent locally enhances convective activity over this region and drives the Walker circulation across the Pacific. Ortland and Alexander (2014) emphasize the significant impact of the planetary-scale variation in convection on tropical upwelling and the TTL annual cycle. A simple way to approximate zonal asymmetries in tropical SSTs in MiMA is to include a zonal wave-like heating/cooling structure at the surface. Physically, this is equivalent to adding a purely zonal heat flux within the mixed layer of the tropics. We give the heat flux a sinusoidal structure:

$$\nabla \cdot \mathbf{F}_W(\lambda, \phi) = \begin{cases} 0, & |\phi| > \phi_w \\ \left[1 - \left(\dfrac{\phi - \phi_0}{\phi_w} \right)^2 \right] Q_W \cos(k_w \lambda - \lambda_0), & |\phi| \leq \phi_w, \end{cases} \tag{3}$$

where Q_W is the warm pool heat flux in $\mathrm{W \, m^{-2}}$, $k_w = 1$ the warm pool wavenumber, and $\phi_w = 20°$ the warm pool width. Also, ϕ_0 and λ_0 can be used to change the meridional position and/or zonal phase, but are set to zero here.

The term Q_W is one of the key parameters in this study, and integrations with the tropical heat flux are denoted by Wx, where x is the value of Q_W in $\mathrm{W \, m^{-2}}$. Tropical SSTs vary by approximately 3 K in integration W30, which is most comparable to the observed zonal

variation in tropical SSTs. The SST asymmetry is roughly linear with Q_w, such that the integration with $Q_W = 15\,\mathrm{W\,m^{-2}}$ exhibits a 1.5° peak-to-peak variation, etc. The associated variation in convection is much more nonlinear, saturating with increasing asymmetry in SSTs. The zonal peak-to-peak variation of convective precipitation is approximately 12%, 19%, and 20% of the zonal mean for 15, 30, and 45 W m^{-2} flux amplitudes.

As explored by Ryu and Lee (2010) in a dry dynamical core, zonal asymmetry in convective heating has a large impact on upwelling in the TTL, and consequently on the cold point height and temperature. Figure 4a shows that localized convective heating lifts and cools the cold point, the effect driven by a substantial increase in upwelling throughout the TTL. In our control simulation, CTRL, the cold point is biased low and warm relative to ECWMF reanalyses and the CMAM30 dataset (a comprehensive model nudged by reanalyses, to provide better vertical resolution of the TTL; Hegglin et al. 2014). This is in part associated with a cold bias in the upper troposphere (the lapse rate in MiMA is too strong, as a result of the idealized convection scheme). More realistic zonal structure in tropical SSTs—the W30 integration in particular—helps alleviate the bias in the lapse rate and lift the cold point much closer to its observed value. As we will discuss later, planetary equatorial waves play an important role here (Gill 1980; Norton 2006; Kerr-Munslow and Norton 2006).

b. Planetary waves in the extratropics

Gaussian-shaped mountains are introduced to the model's Northern Hemisphere to generate extratropical planetary waves. Following Gerber and Polvani (2009), the mountains are centered at about 45° to optimize interaction with the surface westerlies (but we avoid the "valleys" associated with simple wave-1 and -2 topography in that study). Here, wave 1 (wave 2) is excited by the addition of a single mountain (pair of mountains), in the latter case positioned 180° apart in the zonal direction. Each mountain has a height of either 2 or 4 km, and a half-width of 20 degrees in latitude, and 40 (20) degrees in longitude for single mountain (pair of mountains). The values of these two parameters are denoted in integration titles by OxMy, where x is height (in km) and y the wavenumber.

Extratropical planetary waves accelerate the Brewer–Dobson circulation and weaken the climatological polar vortex (Fig. 1). As in the observed atmosphere, the weakening of the climatological vortex is the consequence of aperiodic sudden stratosphere warming (SSW) events. SSWs in MiMA occur with both M1 and M2 orographic forcing, and in the configurations explored here, the rate varies strongly between configurations
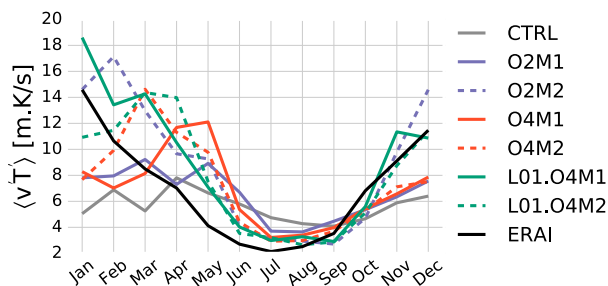

FIG. 5. Seasonal variation of meridional heat flux $\overline{v'T'}$ at 100 hPa and averaged 30°–90°N. The addition of 4-km wave-2 Gaussian mountains in the midlatitudes allows for a very realistic variation in stationary wave forcing when compared to ERA-Interim. Adding land–sea contrast enhances the seasonal cycle even further.

(from zero to about six SSWs per decade). Note that the SSW rate is further influenced by the treatment of gravity wave drag and ozone. For example, in our default configuration, we have symmetrized the ozone between the two hemispheres, such that the Northern Hemisphere has too little relative to observations, and hence a stronger vortex.

To calibrate MiMA relative to the observed atmosphere, we compare the annual cycle of the extratropical average 100-hPa meridional heat flux (a proxy for vertical wave propagation into the stratosphere) in MiMA against ERA-I in Fig. 5. In the zonally symmetric control integration (gray), upward wave activity is weak, with a muted annual cycle consistent with the muted annual cycle in temperature gradients associated with the thick mixed layer. The addition of midlatitude topography (orange curves) dramatically increases wave propagation in the winter, but also helps reduce it in the summer. Wave-2 topography appears more effective in generating upward propagating wave activity, reaching levels on par with ERA-I.

As shown in Fig. 4b, topography cools the cold point region by up to about 1 K, but with little impact on its height. We also find that the cooling is not linear with the amplitude of topography at the surface. Curiously, there is more cooling of the TTL with 2-km topography than 4-km topography for both wave 1 and 2. Figure 5 suggest that the wave activity may saturate relatively quickly in MiMA, in contrast to the dry dynamical core explored by Gerber (2012), where larger topography induced more cooling.

c. The annual cycle of synoptic variability

The heat capacity of the mixed layer strongly influences the amplitude and phase of the annual cycle in meridional temperature contrast, and hence the synoptic variability. As shown in Fig. 6, our control integration (with an equivalent mixed layer depth of 100 m)
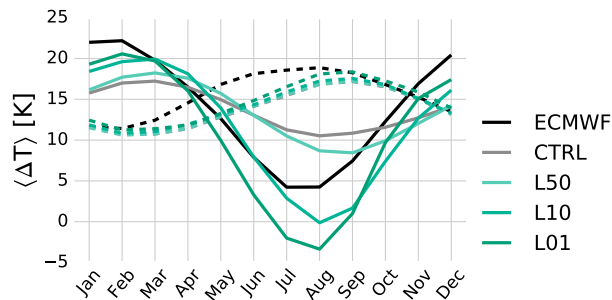
FIG. 6. The monthly variation of the temperature difference between the equator and 45°N(S) for continuous (dotted) lines, averaged over the depth of the troposphere (1000 to 250 hPa). The mixed layer in CTRL is everywhere equivalent to 100 m of seawater, but reduced to 50-, 10-, and 1-m depth between 40° and 50°N in the integrations L50, L10, and L01, respectively.

exhibits a weak annual variation in baroclinicity, comparable to that of the observed Southern Hemisphere, albeit lagged 1–2 months behind from March to August. To approximate the influence of boreal landmass on the annual cycle, we reduce the heat capacity of the mixed layer in the Northern Hemisphere, thereby increasing the annual cycle in baroclinicity and synoptic eddy activity.

MiMA allows one to modify the heat capacity locally across multiple square latitude–longitude patches, or to link it to topographic height (and so more directly connect large-scale topography with land). For simplicity, however, in this study we simply insert a band of reduced heat capacity to the Northern Hemisphere:

$$C_0(\lambda, \phi) = \begin{cases} C_0^l, & \phi_1 \le \phi \le \phi_2, \\ C_0^s, & \text{otherwise} \end{cases} \quad (4)$$

where C_0^l is the heat capacity of "land" and C_0^s is the default "oceanic" heat capacity. The band of land is bounded by $\phi_1 = 40$ and $\phi_2 = 50°$N in all integrations, but earlier experimentation suggested that results are not too sensitive as long as the band covers the central midlatitudes.

The term C_0^l is a key parameter varied in this study, and denoted in integration titles by Lx, where x is the equivalent depth of the mixed layer in meters; for example, L01 corresponds to an integration where the heat capacity of the land is equivalent to 1 m of seawater, 100 times smaller than the default value. Although we refer to this as land–sea contrast, the band is only landlike in that it has a reduced heat capacity. In every other way it is treated exactly as the rest of the mixed layer (i.e., the surface never dries up and still provides an infinite reservoir of water vapor to the atmosphere). It could also be modified by a Q flux in the mixed layer, but in our integrations the flux decays exponentially with latitude,

and reaches trivial values by 40°N. The surface could be made more landlike by reducing the exchange coefficients for moisture and heat between the surface and atmosphere and modifying the albedo, but for our purposes we found that the heat capacity impact was sufficient.

Referring back to Fig. 5, there is a tendency for a lag in the annual cycle in MiMA, especially with wave-1 topography. This is associated in part with the deep mixed layer depth of 100 m in the control configuration. It improves in our integrations where the equivalent mixed layer depth is reduced to approximate land (green curves), quite markedly for wave-1 topography.

Figure 6 illustrates the effect of the heat capacity on the annual cycle of baroclinicity. Here, baroclinicity is defined as the temperature difference between the equator and 45°N/S, averaged between 1000 and 250 hPa. Reducing the heat capacity amplifies the annual cycle in baroclinicity, both increasing it in the winter months and decreasing it in the summer. As in the observed Northern Hemisphere, however, the latter effect is greater: compared to the austral hemisphere, the baroclinicity of the atmosphere collapses in the boreal summer, to a value of 1/4 the annual mean of the austral hemisphere in ERA-I, as compared to a 50% increase in winter. In general, the temperature gradient is a bit weaker in MiMA relative to observations, but captures the right annual variation with an equivalent mixed layer depth of 10 m or less. As noted above, the reduced heat capacity also brings the annual cycle closer to that of the solar forcing, reducing the 2-month lag in the CTRL integration.

Once the albedo is corrected, modification of the Northern Hemisphere temperature gradient has very little impact on the annual mean TTL. Figure 4c even shows a slight warming of the TTL temperatures, particularly right at the cold point, but the change is small compared to those induced by the warm pool or topography. While the hemispheric asymmetry in baroclinicity appears inconsequential to the mean TTL, we show in the next sections that it is perhaps most critical for generating the annual cycle.

4. The annual cycle of the TTL

Figure 7 illustrates the impact of each surface perturbation on the annual cycle in the cold point region. Since the addition of a purely zonal heat flux in the "warm pool" integrations does not break the north–south symmetry of the control climate, there should be no annual cycle in the warm pool integrations. The slight deviations illustrated in Fig. 7a thus provide a rough measure of the sampling error associated with 10 years
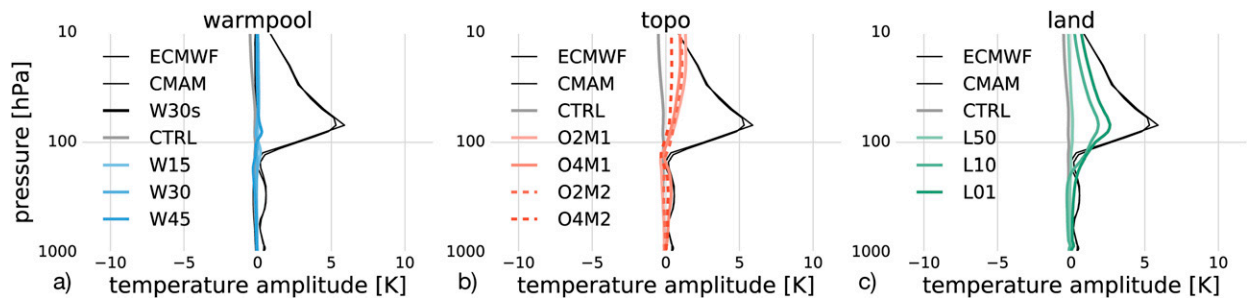
FIG. 7. Vertical profile of the tropical temperature seasonal cycle (JJA mean minus the DJF mean, averaged from 30°S to 30°N) for single parameter scans of (a) tropical warm pool strength, (b) midlatitude topography, and (c) midlatitude "land" mixed layer depth. Mixed layer depth is labeled LD, where D is the mixed layer depth in meters ($D = 100$ m for CTRL). Topography is labeled OHMm, where H is the height in km, and m the wavenumber ($H = 0$ km for CTRL). Warm pool strength is labeled WQ, where Q is the zonal heat flux in W m^{-2} ($Q = 0$ W m^{-2} for CTRL). As expected, the tropical warm pool does not induce a seasonal cycle, as there is no north–south asymmetry in the forcing. Topography does create a seasonal cycle, but mostly in the upper stratosphere, and the profile is qualitatively very different to reanalysis. In contrast, midlatitude land–sea contrast ("land") has an effect that is qualitatively correct, although weak.

of data collection. The TTL does exhibit a weak semi-annual cycle in these integrations, which is modulated by the presence of zonal asymmetry (not shown).

a. Single parameter sweeps: The impact of topography versus baroclinicity

The addition of topography to the boreal hemisphere breaks the north–south symmetry of MiMA, but as seen in Fig. 7b, by itself, it is insufficient to generate the structure and amplitude of the TTL annual cycle. There is a modest effect in the middle to upper stratosphere, which does carry the expected sign: enhanced wave activity in boreal winter drives a stronger Brewer–Dobson circulation, cooling the TTL in boreal winter (Yulaeva et al. 1994). This effect, however, is well above the cold point, which regulates stratospheric water vapor.

Note that we have also optimized the definition of "winter" versus "summer" to construct Figs. 7b and 8, taking into account the phase lag of the annual cycle in MiMA shown in Fig. 5. While the annual cycle is defined by a straightforward June–August (JJA) minus December–February (DJF) difference for all other integrations, for O4M1, summer is defined as July–September (JAS) and winter March–May (MAM), and for O4M2, summer is JAS and winter January–March (JFM). This shift was only applied to the O4M1 and O4M2 integrations (here and in subsequent figures) and the impact of topography alone would appear even weaker if we simply considered the JJA − DJF difference.

For this null result, it is important to remember that topography alone does drive a pronounced annual cycle in upward wave activity in the extratropics in MiMA, with an amplitude comparable to that in reanalyses (Fig. 5). Consistent with other idealized modeling studies (e.g., Chen and Sun 2011; Gerber 2012), we find

that these large planetary waves play an important role in the deep Brewer–Dobson circulation but are drowned out by synoptic and planetary waves that break in the lower stratosphere. As noted by Ueyama et al. (2013), only about 1/5 of the mass that rises above 100 hPa between 15°S and 15°N actually makes it to 70 hPa. It is thus easy for extratropical waves to dominate the mean and annual cycle of upwelling in the middle to upper stratosphere, but they play only a minor role in the cold point region.

Figure 7c finally hints that MiMA is capable of capturing the observed annual cycle in TTL temperatures, and that the annual cycle of synoptic variability plays a key role, as suggested by Jucker et al. (2013). Halving the heat capacity (integration L50) has little effect on the annual cycle (consistent with the weak impact on the baroclinicity shown in Fig. 6), but once it is reduced by a factor of 10 (integration L10), a pronounced annual cycle appears with nearly the same structure as in observations, albeit less than half the amplitude. Further reduction of the mixed layer by another factor of 10 (integration L01) only modestly increases the amplitude, suggesting that the effect has saturated.

While the annual cycle of baroclinicity alone does not fully capture the amplitude of TTL variability, the structure is remarkably similar: temperatures are virtually constant through the depth of the troposphere, with an annual cycle appearing just about the tropical tropopause, increasing sharply to a peak above the cold point, and then decaying linearly with height above. As discussed in the context of Fig. 6, the key appears to be the near collapse of the baroclinicity (and hence synoptic activity) in boreal summer.

In MiMA, the heat capacity of the Southern Hemisphere maintains the baroclinicity year around; in the
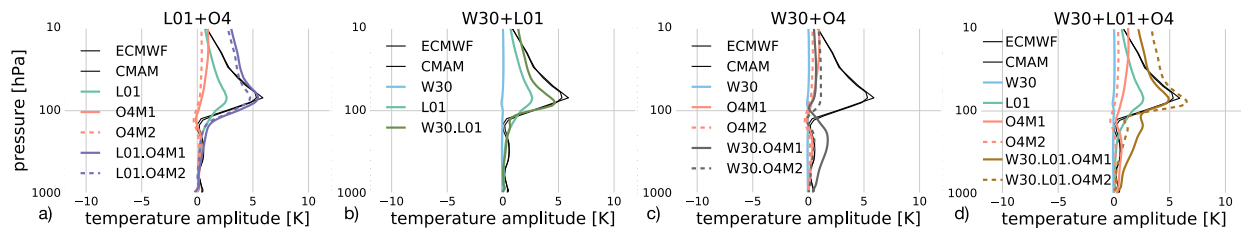
FIG. 8. Vertical profile of tropical temperature seasonal cycle (30°S–30°N) as in Fig. 7, but for mixed parameter scans of (a) midlatitude land–sea contrast and topography, (b) midlatitude land–sea contrast and tropical warm pool, (c) tropical warm pool and midlatitude topography, and (d) tropical warm pool, midlatitude land–sea contrast, and topography. Adding topography or a tropical warm pool to land–sea contrast more than doubles the seasonal cycle, even though topography itself does not have a strong influence, and the warm pool has no effect by itself. Indeed, only adding those two forcings together [see (c)] does not have any significant effect on the TTL annual cycle. Adding all three forcings together has the strongest effect, and the forcing case with tropical warm pool, land–sea contrast, and wave-2 topography (W30.L01.O4M2) even surpasses the annual cycle in reanalysis [dotted brown line in (d)].

real atmosphere, it is the thermal inertia of the Southern Ocean and Antarctica, combined with the latter's strong albedo. Hence the annual cycle of the boreal hemisphere imprints itself on the tropics above the tropopause. The stronger boreal winter circulation drives enhanced upwelling and cools the TTL in this season, but the chief perturbation is the near collapse of the boreal summer circulation, which leads to more substantial warming in the TTL. This results in the net warming of the TTL seen in Fig. 4c.

b. The importance of nonlinear interactions

The three perturbations to the surface in MiMA are not fully independent of one another. For example, the change in the temperature gradients induced by changes in the heat capacity of the slab ocean is associated with variation in subtropical and extratropical jets, which in turn modify planetary wave generation and propagation. Indeed, Fig. 5 shows that planetary wave propagation into the stratosphere is enhanced in the integrations with reduced boreal hemisphere heat capacity, particularly in the one-mountain configuration.

Figure 8 illustrates integrations with various combinations of the separate forcings shown in Fig. 7. It reveals strong nonlinear impacts of the forcings on the annual cycle of the TTL. Planetary-scale waves excited from both the tropics and midlatitudes can more than double the impact of the annual cycle in midlatitude baroclinicity, producing an annual cycle much larger than the sum of the responses to each forcing alone. MiMA can approximate the annual cycle of TTL temperatures in a number of configurations.

Figure 8a explores the nonlinearity between extratropical planetary waves and baroclinicity. Wave-1 or -2 orography more than doubles the annual cycle induced by synoptic variability in the cold point region, bringing the amplitude right to observed levels. The relative amplification becomes even greater at height, and the

annual cycle in MiMA eclipses that of observations above ~50 hPa.

Figure 8b shows the nonlinear amplification associated with tropical planetary waves. In the presence of a warm pool, the annual cycle induced by synoptic variability is also doubled, but only in the region just above the cold point. This indicates that any planetary wave has a pronounced impact in the lower stratosphere, but that the structure differs. The influence of extratropical waves penetrates higher up in the middle to upper stratosphere than that of equatorially forced waves.

The variation in baroclinicity, however, is essential to the annual cycle in MiMA. Figure 8c shows that the weak Northern and Southern Hemispheric asymmetry induced by extratropical topography is relatively unaffected by further zonal asymmetry in the tropics. There is further potential for amplification with all three forcings, as seen in Fig. 8d. In all these cases, the relative phasing between the mountains and "warm pool" could be important, and further experimentation (not shown) revealed that these configurations optimized the impact on the annual cycle. In particular, the curious introduction of an annual cycle in *tropospheric* temperatures seen in the W30.O4M1 and W30.O4M1.L01 integrations is sensitive to the phasing.

Integration W30.L01.O4M2 is notable for producing an annual cycle in TTL temperatures that eclipses that of observations at nearly all levels. This integration combines realistic zonal variation in tropical temperatures (induced by a $30\,W\,m^{-2}$ Q flux), realistic variation in midlatitude baroclinicity (associated with a mixed layer equivalent to 1 m of seawater), and realistic extratropical wave propagation (induced by two 4-km mountains). The annual cycle here does include a radiative contribution associated with water vapor—a "tape recorder" in water vapor (Mote et al. 1996) appears in all MiMA integrations with an annual cycle in cold point temperature—but not from ozone, which is held fixed.
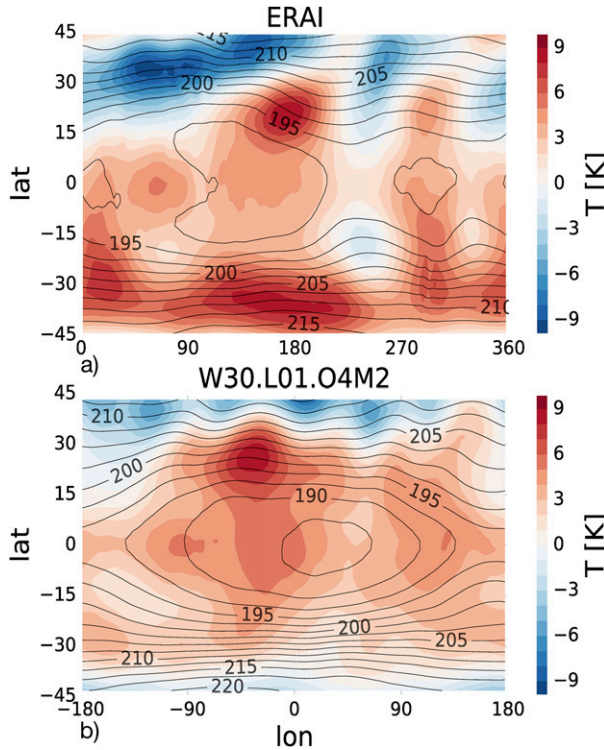
FIG. 9. Longitude–latitude contours of annual mean temperature (contours) and seasonal cycle (shading) at 100 hPa, for (top) ERA-Interim and (bottom) MiMA. Note the strong similarities in structure, and in particular the localized maximum just off the cold point.

Before we dive into the mechanism, Fig. 9 compares the horizontal structure of the TTL and its annual variation in reanalyses with this W30.L01.O4M2 integration, focusing at 100 hPa. The model exhibits a very strong cold trap, which largely mirrors the SST maximum below, and the wave-2 signature associated with midlatitude topography appears in the annual variation of temperatures. But as in ERA-I, there is a great deal of synoptic-scale variation in temperatures, particularly in the annual cycle. This suggests that a mix of planetary and synoptic waves is involved in the mechanism.

5. The mechanism(s) governing the TTL annual cycle

Figure 8 indicates that MiMA can capture a realistic annual cycle of TTL temperatures and upwelling under several very different configurations. Clearly our planet has one specific surface configuration, but the model results suggest that the mechanism may be fairly generic, and not overly sensitive to the exact distribution of continents.

The annual cycle appears just above the tropical tropopause, peaking above the cold point. Below, the

atmosphere is in a Hadley cell regime, where the circulation homogenizes the angular momentum and, to a lesser extent, temperature. Above the tropopause, however, it quickly transitions to a downward control regime, where a (quasi)steady circulation requires wave breaking to transport mass across surfaces of constant angular momentum, and the temperature largely responds to the mechanically induced upwelling. For this latter regime, we can construct a zeroth-order model for the annual cycle by taking a Boussinesq approximation and treating all radiative processes as Newtonian relaxation:

$$\frac{db}{dt} - wN^2 = \frac{b - b_{eq}}{\tau}, \tag{5}$$

where b is the buoyancy (proportional to the temperature), b_{eq} is the "radiative equilibrium" state, w the vertical velocity, N^2 the stratification (which we take to be constant), and τ the effective radiative damping time scale.

As the annual cycle is longer than the radiative damping time scale, we can consider a quasi-steady state where the horizontal advection of buoyancy is small. Then, the temperature perturbation

$$T' \propto b - b_{eq} = -wN^2\tau. \tag{6}$$

Suppose that the annual cycle is set by w (as b_{eq} would not have an *annual* cycle except for radiative effects due to variations in ozone and water vapor) but that the seasonal variations in w are fairly uniform in height [i.e., that the mass flux always decays exponentially with height, as in the leaky pipe model of Neu and Plumb (1999)]. Then, the vertical structure of the temperature perturbation is determined by τ, which has a pronounced vertical structure, decaying from a global maximum of 40 days right above the tropopause to about 10 days in the upper stratosphere (Newman and Rosenfield 1997; Jucker et al. 2013).

This toy model suggests that the radiative structure of the stratosphere will produce a local maximum in the annual cycle of TTL temperature above the tropopause in response to fairly uniform perturbations in the upwelling, as reasoned by, for example, Randel et al. (2002). Or, in other words, a very generic annual cycle in wave breaking could be sufficient to produce such sharp vertical structure in the annual cycle, and help explain why MiMA appears able to capture a fairly realistic annual cycle in several different configurations.

Clearly, the vertical structure of the upwelling does vary depending on the source of wave forcing, as indicated in Fig. 8. The annual cycle in upwelling
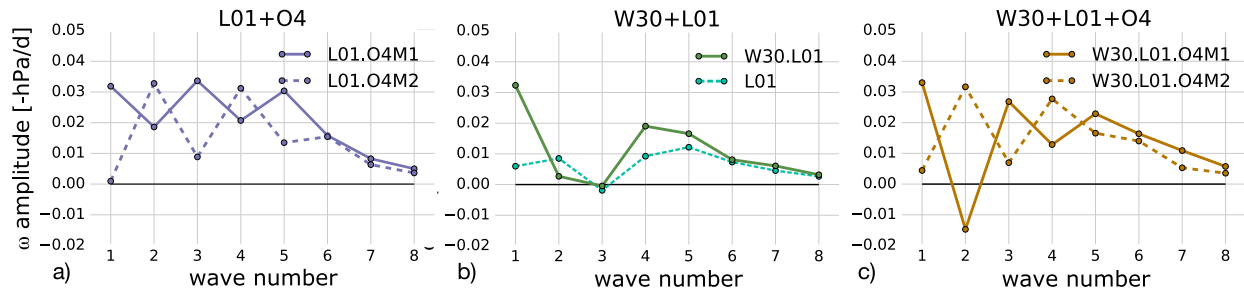
FIG. 10. The annual cycle of tropical upwelling, decomposed into the contribution by each wavenumber, for integrations with (a) land–sea contrast and orography, (b) land–sea contrast alone or with a warm pool, and (c) all three forcings. In (a), odd (even) wavenumbers dominate for the cases with one mountain (two mountains), while in (b) the warm pool dramatically increases the role of wave 1. In (c), W30 + L01 + O4M2 is very similar to L01 + O4M2, plus a small increase in wave-1 forcing, whereas W30 + L01 + O4M1 shows more complex (nonlinear) behavior. Here wave 2 actually counteracts the annual cycle in tropical upwelling.

associated with extratropical topography (Fig. 8a) is substantially deeper than that associated with tropical planetary waves associated with the warm pool (Fig. 8b), producing a larger variation in temperatures at height. The fingerprint associated with tropical waves best matches that in reanalysis, indicating that asymmetry in tropical SSTs is essential for MiMA to capture both the mean and annual cycle of the TTL structure.

The question posed in the introduction remains: What controls the annual cycle in upwelling? The downward control framework allows us to focus in on the waves driving. In Fig. 10, we follow Kim et al. (2016) to decompose the tropical upwelling between 30°S and 30°N into contributions by wavenumber based on momentum and mass conservation (Randel et al. 2002). The plots indicate that the actual waves driving the annual cycle in MiMA vary considerably (albeit somewhat predictably) with the structure of the forcing, despite having a similar overall impact on the upwelling.

With just a perturbation to the Northern Hemisphere heat capacity, synoptic waves play the dominant role (Fig. 10b), but with some help from waves 1 and 2; note that wave 3, the dominant player in the observed annual cycle (Kim et al. 2016), is notably absent. With the addition of a wave-1 warm pool, wave 1 takes on a far more prominent role, but waves 4 and 5 are also amplified. With one large mountain in the midlatitudes, odd-numbered waves (1, 3, and 5) become quite important, whereas with two smaller mountains waves 2 and 4 are amplified (Fig. 10a).

There is a hint of linearity in integrations with all three forcings, with the warm pool amplifying wave 1 with both topographic configurations, but the response is far from strictly linear. Most curiously, upwelling associated with wave 2 tends to oppose the annual cycle when the warm pool and single mountain are combined.

The role of wave 3 in the observed atmosphere may follow in part from the wave-3 structure of the boreal winter flow. Wave 3 does play the most important role in our L01.O4M1 integration, and we suspect this could be further amplified with a more realistic lower boundary. In terms of the mechanism, however, we want to focus on how the impact of hemispheric asymmetry in "land" heat capacity is greatly amplified by the presence of *any* planetary-scale perturbation at the lower boundary.

The source of extratropical stationary planetary wave activity does fluctuate on an annual basis (as it depends on near-surface winds and stability), but there is little fluctuation in the tropical convection associated with the warm pool anomalies. Both, however, leave a strong imprint on the upwelling when combined with boreal heat capacity perturbation. As argued by Ortland and Alexander (2014), this suggest that it is annual variations in wave propagation, more so than the wave source, that cause the annual cycle in wave breaking.

Given the westward intrinsic phase velocity of Rossby waves, stationary waves depend on westerly flow to propagate, and will dissipate when they reach a level of zero velocity, or critical line. Motivated by Ortland and Alexander (2014), we illustrate the annual cycle of the tropical winds and Eliassen–Palm (EP) flux divergence in Fig. 11, taken from our integration with the largest annual cycle in the TTL. (This is the same integration pictured in Fig. 9.) The dotted lines highlight $\overline{u} = 0$ contours, the critical lines for stationary waves. The upper critical line is most relevant, as planetary waves are actively forced in the upper troposphere by tropical convection, and extratropically forced planetary waves can propagate equatorward across the subtropical jets. Indeed, the solid (positive) and dashed (negative) contours for EP flux divergence show one-sided convergence in NH summer, but north–south symmetric convergence in NH winter, causing total wave forcing in the tropics to be larger in the latter.

There is little variation in the austral hemisphere, where the deep mixed layer limits the variability of
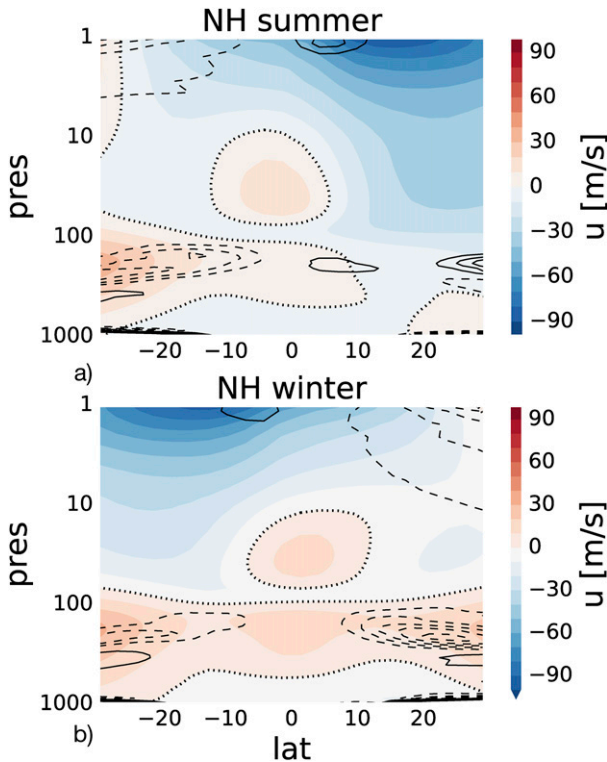
FIG. 11. Latitude–pressure contours of tropical zonal mean zonal wind and total EP-flux divergence in Northern Hemisphere (top) summer and (bottom) winter, based on integration W30.L01. O4M2. This is the integration with the largest seasonal cycle in the TTL. The thick black dotted line denotes $u = 0$ (i.e., critical lines for stationary Rossby waves). The contour interval for the EP-flux divergence is $2 \, \mathrm{m \, s^{-1} \, day^{-1}}$, and dashed (solid) lines indicate convergence (divergence).

surface temperatures. In the boreal hemisphere, however, the subtropical jet collapses in summertime, cutting off any planetary wave activity from this hemisphere. Given the large meridional scale of the planetary waves, however, one must not overinterpret the finescale structure of the critical line. Propagation will depend on the overall state of the tropical atmosphere, and the key is that the boreal winter state will favor a deeper penetration of planetary wave activity into the tropical stratosphere than the boreal summer state, even if the wave source remains constant.

We note that MiMA exhibits a small degree of superrotation in the UTLS. (This can also be seen in Fig. 1.) These westerlies are localized in the deep tropics, and may bias the climatological mean propagation of waves. Net TTL upwelling, however, depends most critically on the wave driving at the turning latitudes, near 30°S and 30°N, and so on the winds in the subtropics. The superrotation is also fairly constant in time, and so has little impact on the annual cycle in upwelling.

Figure 12 compares the tropical mean winds of the two solstitial seasons across a number of configurations, focusing on the region of the upper critical line. We take an average from 30°S to 30°N, as this corresponds to the region of upwelling (i.e., spans the two turning latitudes of the residual mean circulation). The broad average captures the influence of the subtropical jets; for this reason the troposphere appears to be in a rather strong westerly regime below 120 hPa in all configurations. The darker lines in Fig. 12f correspond to the winds of the integration depicted in Fig. 11, and more clearly illustrate the fact that westerlies (in a tropical mean sense) extend 30 hPa higher in boreal winter than summer, allowing stationary waves to penetrate that much deeper into the TTL.

The top row of Fig. 12 helps us understand the physical processes controlling the tropical mean winds. Modification of the boreal hemisphere baroclinicity is critical for the annual modification of the winds; the L50 integration in Fig. 12a is comparable to the control integration, and exhibits almost no variation; once the effective mixed layer depth drops to 10 or 1 m, however, the critical line drops markedly in the boreal summer, associated with the weakening of the subtropical jet. In comparison, it does not really change that much in the winter: increasing the baroclinicity does not really affect the tropical winds, as the jets are determined by angular momentum constraints. Varying the midlatitude topography has almost no influence on the winds at this level (Fig. 12b). The introduction of the warm pool (Fig. 12c) has a pronounced effect (consistent with its control on the mean state of the TTL), but cannot by itself generate an annual cycle.

The bottom row of Fig. 12 illustrates the potential for nonlinearity as the forcings are combined. The situation is fairly linear when a warm pool is combined with the boreal heat capacity modification, integration W30.L01 in Fig. 12e. The wind profile takes on that of the warm pool integration (W30), but fluctuates in height just as in the L01. Topography—the two-mountain configuration in particular—enhances the annual cycle of the winds associated with the fluctuation of baroclinicity by up to a 50% (Fig. 12d). This enhancement extends to the integrations with all three forcings (Fig. 12f), but again the structure of the profile is determined primarily by the warm pool.

To complete the argument, Fig. 13 illustrates the link between the seasonal variation of the tropical zero wind line and the seasonal variation of TTL temperatures across all integrations. The positive slope implies that the larger the height difference of the zero wind crossing between DJF and JJA, the larger the TTL temperature difference between these seasons. As illustrated in
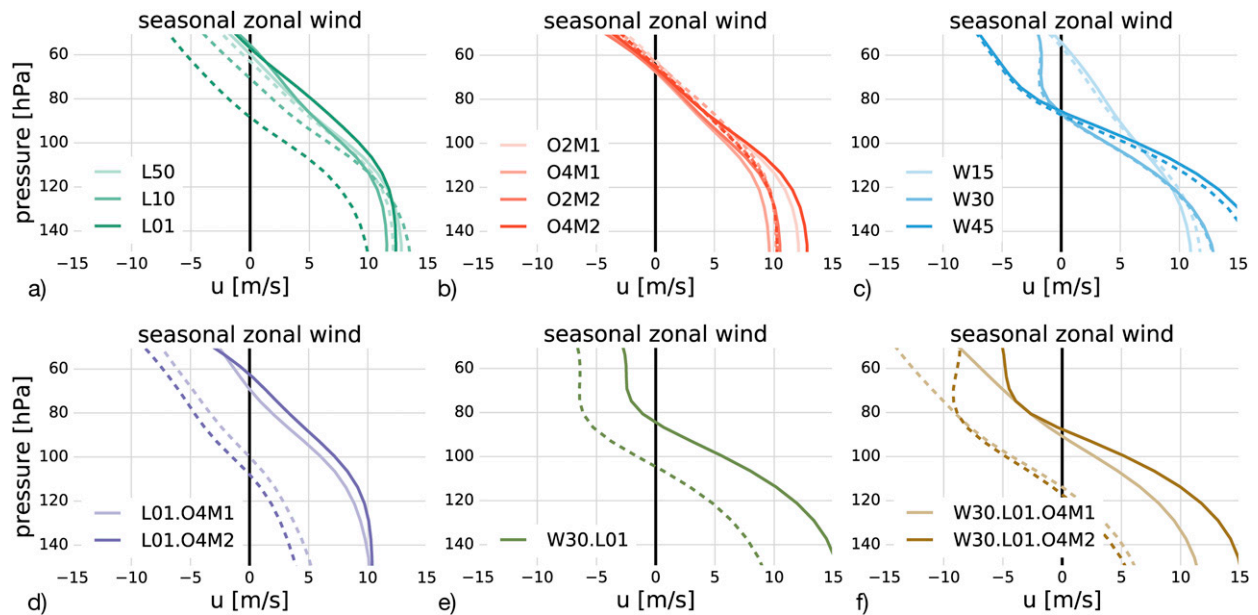
FIG. 12. Annual cycle of tropical zonal mean zonal wind profiles for parameter scans in (a) midlatitude land–sea contrast, (b) midlatitude topography, and (c) tropical warm pool, and the mixed cases (d) land–sea contrast plus topography, (e) tropical warm pool plus land–sea contrast, and (f) tropical warm pool plus land–sea contrast plus topography. Solid (dashed) lines denote DJF (JJA). The strength of the annual cycle in tropical zonal mean zonal wind profile is directly related to the strength of the annual cycle in temperature (Figs. 7 and 8).

Fig. 11, the seasonal variation in the critical line is primarily associated with the weakening of the Northern Hemisphere subtropical jet in boreal summer, which prevents stationary Rossby waves from penetrating into the TTL, leading to weak wave breaking, diminished upwelling, and warmer temperatures in this season.

Overall, 77% of the variation in seasonal TTL temperatures can be explained by the seasonal variation in the critical lines. The critical line was assessed between 30°S and 30°N (consistent with Fig. 12), to capture the full width of the tropical upwelling region. Further experimentation with different widths (not shown)
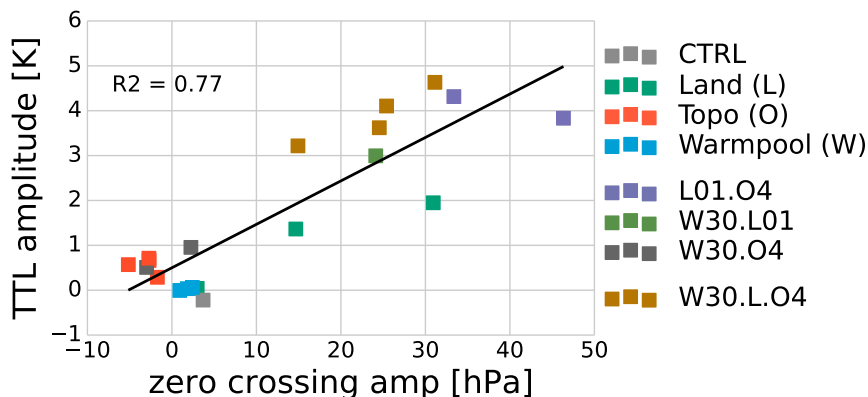

FIG. 13. The amplitude of the annual cycle in TTL temperature, plotted as a function of seasonal variation in the critical line. The significant correlation, $R^2 = 0.77$, suggests that the zonal wind structure strongly determines the location of wave propagation and breaking, and hence, tropical upwelling. The TTL annual cycle is quantified by the difference between JJA and DJF in mean temperature over the tropics and between 120 and 20 hPa. The critical line annual cycle is quantified by the difference in the pressure level where the zonal mean zonal wind, averaged from 30°S to 30°N, changes from westerly to easterly, again JJA vs DJF. The label L01.O4 includes both L01.O4M1 and L01.O4M2, L01.O4 includes both L01.O4M1 and L01.O4M2, and the label W30.L.O4 includes W30.L01.O4M1, W30.L01.O4M2, W30. L01.O2M2, and W30.L10.O4M2.

TABLE A1. List of the main parameter values that were set constant throughout all simulations in this work.

Parameter	Value	Units	Meaning
dt_atmos	600	s	Dynamical time step
num_levels	80	–	Number of hybrid vertical levels
damping_order	4	–	Eighth-order numerical diffusion
water_correction_limit	200	hPa	No water correction above 200 hPa to conserve stratospheric water vapor
initial_sphum	2.0×10^{-6}	$kg\,kg^{-1}$	Initial constant specific humidity throughout the atmosphere
heat_capacity	4×10^8	$J\,K^{-1}\,m^{-2}$	Mixed layer depth of 100 m
slandlon	0	Degrees	Western boundary of land patch
elandlon	360	Degrees	Eastern boundary of land patch
slandlat	40	Degrees	Southern boundary of land patch
elandlat	50	Degrees	Northern boundary of land patch
qflux_amp	30	$W\,m^{-2}$	Meridional Q flux to export heat from tropics to extratropics
olat	45	Degrees	Meridional center of Gaussian mountains
olon	90 (270)	Degrees	Zonal center of Gaussian mountains
wlat	20	Degrees	Meridional half-width of Gaussian mountains
wlon	40 (20)	Degrees	Zonal half-width of wave 1 (2) Gaussian mountains
rhbm	0.7	–	Relax to 70% relative humidity in Betts–Miller convection scheme
ozone_file	ozone_1990.nc	–	Use static, hemispherically symmetric ozone profiles derived from Fortuin and Langematz (1994)
co2_val	300	ppm	Run with 300 ppm CO_2
dt_rad	7200	s	Call RRTM radiation every 2 h
solr_cnst	1360	$W\,m^{-2}$	Solar constant for shortwave radiation

revealed that this range of averaging is almost optimal. The correlation is stronger if we neglect the integrations with only variation in midlatitude baroclinicity (green dots): here no planetary waves are explicitly forced, and must be internally generated through baroclinic instability. With the addition of any source of planetary waves, the annual cycle in critical line variation leads to an amplified TTL annual cycle. (The L01.O4M2 integration—the rightmost dot in Fig. 13—is also anomalous, but here the issue seems to be the large variation in zonal winds, as shown in Fig. 12d, suggesting that the impact may saturate.)

The slope, approximately $0.1\,K\,hPa^{-1}$, indicates that a 10-hPa variation of the critical line translates to a 1-K variation in temperatures. This tends to underestimate the impact, as we did not constrain the regression to cross the origin, and the integrations without any zonal asymmetries exhibit a weaker response. In integrations with a warm pool, the slope is closer to $0.2\,K\,hPa^{-1}$, indicating a larger sensitivity (by a factor of 2) to variation in the critical lines.

6. Summary and conclusions

We have developed a model of an idealized moist atmosphere, constructed to capture the essential elements of the hydrological cycle and radiative processes, but explicitly exclude cloud–radiative feedbacks. The model, detailed in section 2, is designed to fill in the gap between models of the "dry" atmospheric circulation

(e.g., Held and Suarez 1994) and comprehensive aquaplanet models, building on the work of Frierson et al. (2006) and Merlis et al. (2013a).

We used the model to explore the mechanisms regulating the climatology and annual cycle of the tropical tropopause layer (TTL), identifying the key roles of planetary waves and boreal hemisphere temperature gradients. Adiabatic cooling associated with upwelling in the TTL region is responsible for the formation of the tropical cold point. As shown in section 3, the model emphasizes the importance of tropical control over the climatological TTL. Tropical planetary waves drive significant upwelling in the *lower stratosphere*, and so set the temperature and height of the cold point (e.g., Gettelman et al. 2002; Boehm and Lee 2003; Ryu and Lee 2010; Birner and Bönisch 2011; Ortland and Alexander 2014; Kim and Alexander 2015). Extratropical planetary waves associated with large-scale orography play a first-order role in the circulation and variability of the stratosphere above 70 hPa (e.g., Yulaeva et al. 1994; Plumb 2002; Ueyama and Wallace 2010; Chen and Sun 2011) but are far less effective at modifying the mean TTL compared to tropical planetary waves.

Annual variations in the upwelling are primarily responsible for the annual variations in TTL temperatures. Previous studies have highlighted the potential roles of synoptic-scale waves associated with midlatitude baroclinic zones (Jucker et al. 2013) and planetary-scale waves generated by tropical convection (e.g., Ortland and Alexander 2014) and midlatitude topography (e.g.,

Yulaeva et al. 1994) in driving TTL upwelling. We use the idealized atmospheric model to explore the individual roles of each forcing, and, more importantly, their mutual interactions.

As shown in section 4, the model is able to capture a fairly realistic variation of TTL temperatures in a number of configurations. The key ingredients are 1) a stronger annual cycle in baroclinicity in the boreal hemisphere, associated with reduced heat capacity of land relative to ocean, and 2) the presence of stationary planetary-scale waves, associated with *either* tropical SST variations or midlatitude topography. The critical role of boreal hemisphere baroclinicity emphasizes the potential for extratropical control over the TTL, while the fairly generic response of the TTL is consistent with the results of Randel and Jensen (2013) and Grise and Thompson (2013), who found important roles for all wave types in this region, in addition to considerable variations on a year-to-year basis.

The role of each of these ingredients in driving the annual variation was explored in section 5, where we built on the mechanism for TTL variation proposed by Ortland and Alexander (2014). The stronger temperature variations in the boreal hemisphere—particularly the weakening of the summertime subtropical jet—lead to a significant lowering of the transition from westerly to easterly flow in boreal summer. Stationary planetary waves cannot effectively propagate through easterly flows, leading to a reduced wave breaking in boreal summer, and consequently, a warming of the TTL region. Figure 13 suggests that 75% of the seasonal variability in the TTL temperatures across all of our simulations is associated with the variation of the tropical winds. Variation in boreal baroclinicity associated with the reduced heat capacity in the Northern Hemisphere was essential for varying the tropical winds, but planetary-scale waves double the impact on TTL temperatures.

Our results suggests that the signature of tropical planetary waves is shallower than that of extratropical planetary waves, such that the tropical forcing generates a vertical profile of temperature variations closest to that seen in reanalyses and more comprehensive GCMs. The steep drop in effective radiative relaxation rates with height, however, will tend to concentrate the annual cycle in temperatures just above the tropopause. Hence the model captures a fairly realistic annual variation in TTL temperatures over a number of very different configurations, even without a tropical warm pool.

We acknowledge the danger of overinterpreting results from an idealized model that explicitly omits processes (e.g., clouds) that play a critical role in the climate system. It is the robustness of the response to a number of very

different configurations that gives us confidence in the relationship between planetary waves, midlatitude baroclinicity, and the TTL annual cycle.

In closing, we emphasize that, in the spirit of Held and Suarez (1994), MiMA has been defined as a recipe for an idealized atmosphere, rather than a specific numerical implementation. One can compare the influence of numerics by changing the underlying dynamical core, or the impact of the representation of radiation by changing the radiative transfer scheme, e.g., RRTM versus AM2. We therefore believe it may be well suited for other applications that involve the interactions between moisture, radiation, and large-scale dynamics.

APPENDIX

Model Setup Parameters

All input files are part of the data published in Jucker and Gerber (2017) and available online. A detailed list of parameters in MiMA and their default values can be found in the documentation folder of the code repository (Jucker 2017) and online at https://mjucker.github.io/MiMA. In addition, Table A1 gives the most important model setup parameters, which are set to the same values for all simulations listed in Table 1.

REFERENCES

Abalos, M., F. Ploeger, P. Konopka, W. J. Randel, and E. Serrano, 2013: Ozone seasonality above the tropical tropopause: Reconciling the Eulerian and Lagrangian perspectives of transport processes. *Atmos. Chem. Phys.*, **13**, 10 787–10 794, doi:10.5194/acp-13-10787-2013.

Atticks, M. G., and G. D. Robinson, 1983: *Quart. J. Roy. Meteor. Soc.*, **109**, 295–308, doi:10.1002/qj.49710946004.

Betts, A. K., 1986: A new convective adjustment scheme. Part I: Observational and theoretical basis. *Quart. J. Roy. Meteor. Soc.*, **112**, 677–691, doi:10.1002/qj.49711247307.

——, and M. J. Miller, 1986: A new convective adjustment scheme. Part II: Single column tests using GATE wave, BOMEX, ATEX, and Arctic air-mass data sets. *Quart. J. Roy. Meteor. Soc.*, **112**, 693–709, doi:10.1002/qj.49711247308.

Birner, T., and H. Bönisch, 2011: Residual circulation trajectories and transit times into the extratropical lowermost

stratosphere. *Atmos. Chem. Phys.*, **11**, 817–827, doi:10.5194/acp-11-817-2011.

Boehm, M. T., and S. Lee, 2003: The implications of tropical Rossby waves for tropical tropopause cirrus formation and for the equatorial upwelling of the Brewer–Dobson circulation. *J. Atmos. Sci.*, **60**, 247–261, doi:10.1175/1520-0469(2003)060<0247:TIOTRW>2.0.CO;2.

Brewer, A. W., 1949: Evidence for a world circulation provided by the measurements of helium and water vapour distribution in the stratosphere. *Quart. J. Roy. Meteor. Soc.*, **75**, 351–363, doi:10.1002/qj.49707532603.

Butler, A. H., D. W. J. Thompson, and R. Heikes, 2010: The steady-state atmospheric circulation response to climate change–like thermal forcings in a simple general circulation model. *J. Climate*, **23**, 3474–3496, doi:10.1175/2010JCLI3228.1.

Chae, J. H., and S. C. Sherwood, 2007: Annual temperature cycle of the tropical tropopause: A simple model study. *J. Geophys. Res.*, **112**, D19111, doi:10.1029/2006JD007956.

Chen, G., and R. A. Plumb, 2009: Quantifying the eddy feedback and the persistence of the zonal index in an idealized atmospheric model. *J. Atmos. Sci.*, **66**, 3707–3720, doi:10.1175/2009JAS3165.1.

——, and L. Sun, 2011: Mechanisms of the tropical upwelling branch of the Brewer–Dobson circulation: The role of extratropical waves. *J. Atmos. Sci.*, **68**, 2878–2892, doi:10.1175/JAS-D-11-044.1.

Cohen, N. Y., E. P. Gerber, and O. Bühler, 2013: Compensation between resolved and unresolved wave driving in the stratosphere: Implications for downward control. *J. Atmos. Sci.*, **70**, 3780–3798, doi:10.1175/JAS-D-12-0346.1.

Delworth, T. L., and Coauthors, 2006: GFDL's CM2 global coupled climate models. Part I: Formulation and simulation characteristics. *J. Climate*, **19**, 643–674, doi:10.1175/JCLI3629.1.

Dessler, A. E., M. R. Schoeberl, T. Wang, S. M. Davis, and K. H. Rosenlof, 2013: Stratospheric water vapor feedback. *Proc. Natl. Acad. Sci. USA*, **110**, 18 087–18 091, doi:10.1073/pnas.1310344110.

Fortuin, J. P. F., and U. Langematz, 1994: An update on the global ozone climatology and on concurrent ozone and temperature trends. *Atmospheric Sensing and Modeling*, R. P. Santer, Ed., International Society for Optical Engineering (SPIE Proceedings, Vol. 2311), 207–216.

Frierson, D. M. W., 2007: The dynamics of idealized convection schemes and their effect on the zonally averaged tropical circulation. *J. Atmos. Sci.*, **64**, 1959–1976, doi:10.1175/JAS3935.1.

——, I. M. Held, and P. Zurita-Gotor, 2006: A gray-radiation aquaplanet moist GCM. Part I: Static stability and eddy scale. *J. Atmos. Sci.*, **63**, 2548–2566, doi:10.1175/JAS3753.1.

——, ——, and ——, 2007: A gray-radiation aquaplanet moist GCM. Part II: Energy transports in altered climates. *J. Atmos. Sci.*, **64**, 1680–1693, doi:10.1175/JAS3913.1.

Fueglistaler, S., A. E. Dessler, T. J. Dunkerton, I. Folkins, Q. Fu, and P. W. Mote, 2009: Tropical tropopause layer. *Rev. Geophys.*, **47**, RG1004, doi:10.1029/2008RG000267.

——, P. H. Haynes, and P. M. Forster, 2011: The annual cycle in lower stratospheric temperatures revisited. *Atmos. Chem. Phys.*, **11**, 3701–3711, doi:10.5194/acp-11-3701-2011.

Gerber, E. P., 2012: Stratospheric versus tropospheric control of the strength and structure of the Brewer–Dobson circulation. *J. Atmos. Sci.*, **69**, 2857–2877, doi:10.1175/JAS-D-11-0341.1.

——, and G. K. Vallis, 2007: Eddy–zonal flow interactions and the persistence of the zonal index. *J. Atmos. Sci.*, **64**, 3296–3311, doi:10.1175/JAS4006.1.

——, and L. M. Polvani, 2009: Stratosphere–troposphere coupling in a relatively simple AGCM: The importance of stratospheric variability. *J. Climate*, **22**, 1920–1933, doi:10.1175/2008JCLI2548.1.

Gettelman, A., M. L. Salby, and F. Sassi, 2002: Distribution and influence of convection in the tropical tropopause region. *J. Geophys. Res.*, **107**, 4080, doi:10.1029/2001JD001048.

——, and Coauthors, 2010: Multimodel assessment of the upper troposphere and lower stratosphere: Tropics and global trends. *J. Geophys. Res.*, **115**, D00M08, doi:10.1029/2009JD013638.

Gill, A. E., 1980: Some simple solutions for heat-induced tropical circulation. *Quart. J. Roy. Meteor. Soc.*, **106**, 447–462, doi:10.1002/qj.49710644905.

Grise, K. M., and D. W. Thompson, 2013: On the signatures of equatorial and extratropical wave forcing in tropical tropopause layer temperatures. *J. Atmos. Sci.*, **70**, 1084–1102, doi:10.1175/JAS-D-12-0163.1.

Haqq-Misra, J., S. Lee, and D. M. W. Frierson, 2011: Tropopause structure and the role of eddies. *J. Atmos. Sci.*, **68**, 2930–2944, doi:10.1175/JAS-D-11-087.1.

Hegglin, M. I., and Coauthors, 2014: Vertical structure of stratospheric water vapour trends derived from merged satellite data. *Nat. Geosci.*, **7**, 768–776, doi:10.1038/ngeo2236.

Held, I. M., 2005: The gap between simulation and understanding in climate modeling. *Bull. Amer. Meteor. Soc.*, **86**, 1609–1614, doi:10.1175/BAMS-86-11-1609.

——, and M. M. J. Suarez, 1994: A proposal for the intercomparison of the dynamical cores of atmospheric general circulation models. *Bull. Amer. Meteor. Soc.*, **75**, 1825–1830, doi:10.1175/1520-0477(1994)075<1825:APFTIO>2.0.CO;2.

Highwood, E. J., and B. J. Hoskins, 1998: The tropical tropopause. *Quart. J. Roy. Meteor. Soc.*, **124**, 1579–1604, doi:10.1002/qj.49712454911.

Holton, J. R., P. H. Haynes, M. E. McIntyre, A. R. Douglass, R. B. Rood, and L. Pfister, 1995: Stratosphere–troposphere exchange. *Rev. Geophys.*, **33**, 403–439, doi:10.1029/95RG02097.

Iacono, M. J., E. J. Mlawer, S. A. Clough, and J.-J. Morcrette, 2000: Impact of an improved longwave radiation model, RRTM, on the energy budget and thermodynamic properties of the NCAR Community Climate Model, CCM3. *J. Geophys. Res.*, **105**, 14873–14890, doi:10.1029/2000JD900091.

Jucker, M., 2016: Are sudden stratospheric warmings generic? Insights from an idealized GCM. *J. Atmos. Sci.*, **73**, 5061–5080, doi:10.1175/JAS-D-15-0353.1.

——, 2017: mjucker/mima: Mima v1.0. Accessed 2017, doi:10.5281/zenodo.321708.

——, and E. P. Gerber, 2017: Input files, data and analysis scripts to "Untangling the annual cycle of the tropical tropopause layer with an idealized moist model." Mendeley data v1, accessed 2017, doi:10.17632/jvfdrsyhnk.1.

——, S. Fueglistaler, and G. K. Vallis, 2013: Maintenance of the stratospheric structure in an idealized general circulation model. *J. Atmos. Sci.*, **70**, 3341–3358, doi:10.1175/JAS-D-12-0305.1.

Kerr-Munslow, A. M., and W. A. Norton, 2006: Tropical wave driving of the annual cycle in tropical tropopause temperatures. Part I: ECMWF analyses. *J. Atmos. Sci.*, **63**, 1410–1419, doi:10.1175/JAS3697.1.

Kidston, J., G. K. Vallis, S. M. Dean, and J. A. Renwick, 2011: Can the increase in the eddy length scale under global warming cause the poleward shift of the jet streams? *J. Climate*, **24**, 3764–3780, doi:10.1175/2010JCLI3738.1.

Kim, J., and S.-W. Son, 2015: Formation and maintenance of the tropical cold-point tropopause in a dry dynamic-core GCM. *J. Atmos. Sci.*, **72**, 3097–3115, doi:10.1175/JAS-D-14-0338.1.

——, W. J. Randel, T. Birner, and M. Abalos, 2016: Spectrum of wave forcing associated with the annual cycle of upwelling at the tropical tropopause. *J. Atmos. Sci.*, **73**, 855–868, doi:10.1175/JAS-D-15-0096.1.

Kim, J.-E., and M. J. Alexander, 2015: Direct impacts of waves on tropical cold point tropopause temperature. *Geophys. Res. Lett.*, **42**, 1584–1592, doi:10.1002/2014GL062737.

Konopka, P., J.-U. Grooß, G. Günther, F. Ploeger, R. Pommrich, R. Müller, and N. Livesey, 2010: Annual cycle of ozone at and above the tropical tropopause: Observations versus simulations with the Chemical Lagrangian Model of the Stratosphere (CLaMS). *Atmos. Chem. Phys.*, **10**, 121–132, doi:10.5194/acp-10-121-2010.

Merlis, T. M., T. Schneider, S. Bordoni, and I. Eisenman, 2013a: Hadley circulation response to orbital precession. Part I: Aquaplanets. *J. Climate*, **26**, 740–753, doi:10.1175/JCLI-D-11-00716.1.

——, ——, ——, and ——, 2013b: Hadley circulation response to orbital precession. Part II: Subtropical continent. *J. Climate*, **26**, 754–771, doi:10.1175/JCLI-D-12-00149.1.

Ming, A., A. C. Maycock, P. Hitchcock, and P. Haynes, 2017: The radiative role of ozone and water vapour in the temperature annual cycle in the tropical tropopause layer. *Atmos. Chem. Phys.*, **17**, 5677–5701, doi:10.5194/acp-17-5677-2017.

Mlawer, E. J., S. J. Taubman, P. D. Brown, M. J. Iacono, and S. A. Clough, 1997: Radiative transfer for inhomogeneous atmospheres: RRTM, a validated correlated-k model for the longwave. *J. Geophys. Res.*, **102**, 16663–16682, doi:10.1029/97JD00237.

Mote, P. W., and Coauthors, 1996: An atmospheric tape recorder: The imprint of tropical tropopause temperatures on stratospheric water vapor. *J. Geophys. Res.*, **101**, 3989–4006, doi:10.1029/95JD03422.

Neu, J. L., and R. A. Plumb, 1999: Age of air in a "leaky pipe" model of stratospheric transport. *J. Geophys. Res.*, **104**, 19 243–19 255, doi:10.1029/1999JD900251.

Newman, P. A., and J. E. Rosenfield, 1997: Stratospheric thermal damping times. *Geophys. Res. Lett.*, **24**, 433–436, doi:10.1029/96GL03720.

Norton, W. A., 2006: Tropical wave driving of the annual cycle in tropical tropopause temperatures. Part II: Model results. *J. Atmos. Sci.*, **63**, 1420–1431, doi:10.1175/JAS3698.1.

Ortland, D. A., and M. J. Alexander, 2014: The residual-mean circulation in the tropical tropopause layer driven by tropical waves. *J. Atmos. Sci.*, **71**, 1305–1322, doi:10.1175/JAS-D-13-0100.1.

Ploeger, F., and Coauthors, 2012: Horizontal transport affecting trace gas seasonality in the tropical tropopause layer (TTL). *J. Geophys. Res. Atmos.*, **117**, D09303, doi:10.1029/2011JD017267.

Plumb, R. A., 2002: Stratospheric transport. *J. Meteor. Soc. Japan*, **80**, 793–809, doi:10.2151/jmsj.80.793.

——, 2007: Tracer interrelationships in the stratosphere. *Rev. Geophys.*, **45**, RG4005, doi:10.1029/2005RG000179.

Polvani, L. M., and P. J. Kushner, 2002: Tropospheric response to stratospheric perturbations in a relatively simple general circulation model. *Geophys. Res. Lett.*, **29**, 1114, doi:10.1029/2001GL014284.

Randel, W. J., and E. J. Jensen, 2013: Physical processes in the tropical tropopause layer and their roles in a changing climate. *Nat. Geosci.*, **6**, 169–176, doi:10.1038/ngeo1733.

——, R. R. Garcia, and F. Wu, 2002: Time-dependent upwelling in the tropical lower stratosphere estimated from the zonal-mean momentum budget. *J. Atmos. Sci.*, **59**, 2141–2152, doi:10.1175/1520-0469(2002)059<2141:TDUITT>2.0.CO;2.

——, ——, and ——, 2008: Dynamical balances and tropical stratospheric upwelling. *J. Atmos. Sci.*, **65**, 3584–3594, doi:10.1175/2008JAS2756.1.

Ryu, J.-H., and S. Lee, 2010: Effect of tropical waves on the tropical tropopause transition layer upwelling. *J. Atmos. Sci.*, **67**, 3130–3148, doi:10.1175/2010JAS3434.1.

——, ——, and S.-W. Son, 2008: Vertically propagating Kelvin waves and tropical tropopause variability. *J. Atmos. Sci.*, **65**, 1817–1837, doi:10.1175/2007JAS2466.1.

Schneider, T., and C. C. Walker, 2006: Self-organization of atmospheric macroturbulence into critical states of weak nonlinear eddy–eddy interactions. *J. Atmos. Sci.*, **63**, 1569–1586, doi:10.1175/JAS3699.1.

Schofield, R., S. Fueglistaler, I. Wohltmann, and M. Rex, 2011: Sensitivity of stratospheric Br_y to uncertainties in very short lived substance emissions and atmospheric transport. *Atmos. Chem. Phys.*, **11**, 1379–1392, doi:10.5194/acp-11-1379-2011.

Simpson, I. R., M. Blackburn, and J. D. Haigh, 2009: The role of eddies in driving the tropospheric response to stratospheric heating perturbations. *J. Atmos. Sci.*, **66**, 1347–1365, doi:10.1175/2008JAS2758.1.

Solomon, S., K. H. Rosenlof, R. W. Portmann, J. S. Daniel, S. M. Davis, T. J. Sanford, and G.-K. Plattner, 2010: Contributions of stratospheric water vapor to decadal changes in the rate of global warming. *Science*, **327**, 1219–1223, doi:10.1126/science.1182488.

Ueyama, R., and J. M. Wallace, 2010: To what extent does high-latitude wave forcing drive tropical upwelling in the Brewer–Dobson circulation? *J. Atmos. Sci.*, **67**, 1232–1246, doi:10.1175/2009JAS3216.1.

——, E. P. Gerber, J. M. Wallace, and D. M. W. Frierson, 2013: The role of high-latitude waves in the intraseasonal to seasonal variability of tropical upwelling in the Brewer–Dobson circulation. *J. Atmos. Sci.*, **70**, 1631–1648, doi:10.1175/JAS-D-12-0174.1.

Voigt, A., and T. A. Shaw, 2015: Circulation response to warming shaped by radiative changes of clouds and water vapour. *Nat. Geosci.*, **8**, 102–106, doi:10.1038/ngeo2345.

Yulaeva, E., J. R. Holton, and J. M. Wallace, 1994: On the cause of the annual cycle in tropical lower-stratospheric temperatures. *J. Atmos. Sci.*, **51**, 169–174, doi:10.1175/1520-0469(1994)051<0169:OTCOTA>2.0.CO;2.